

Simulation of a lean direct injection combustor for the next high speed civil transport (HSCT) vehicle combustion systems

By H. El-Asrag, F. Ham AND H. Pitsch

1. Motivation and objectives

Designing commercially viable propulsion systems for supersonic aircraft is a major challenge. All modern combustors must balance the need for stability and performance with the goals of efficiency and cleanliness. These competing demands, however, are exacerbated in supersonic situations where the operating conditions are much more severe. Supersonic transport aircrafts usually fly in the stratosphere, at cruising altitudes around 60,000 – 65,000 ft. The engine emissions produced at such high altitude contribute to depleting the ozone layer. In addition, the high fuel consumption increases the overall cost of operation. For example, the Concorde was powered by turbojet engines that made use of afterburner, a very inefficient combustion system. Next-generation high speed civil transport (HSCT) vehicles will likely be based on low-bypass turbofan, afterburner-free technology. In addition to the foregoing improvements, if the engine emission characteristics and performance are further enhanced, supersonic vehicles may become part of the world's air transportation system.

In this report we focus first on the choice of the engine design and validating our code and initial mesh against LDV data. Many design concepts exist for gas turbine engines. The most well known are the Rich burn-Quick Quench-Lean Burn (RQL), Lean Premix-Prevaporized (LPP), and the Lean-Direct-Injection (LDI) engine. The RQL is designed to operate at ultra-low NO_x emissions. First fuel is burned, under highly rich environment, then quickly quenched with cold air, then finally burned very lean. However, some technical difficulties usually rise with such configurations. If the mixing is not rapid enough, a lot of heat is transferred to the walls, which may cause material problems. In addition, if mixing is not rapid enough, a lot of soot and carbon monoxide (CO) will be emitted at the exhaust of the burner. LPP and LDI on the other hand focus on operating the engine at the near premixed regime, which results in very low NO_x , soot and CO emissions. The air and the fuel droplets are mixed and atomized completely and then premixed in a long tube in the LPP design. The mixing and uniformity of the flow reduce the NO_x emissions but might generate undesirable flame instabilities. Here, a single element LDI configuration is chosen as a precursor for the HSCT engine (Tacina *et al.* (2001); Jun *et al.* (2005); Yang *et al.* (2003)). The air is injected in a swirler of 60 degree vanes, where it mixes, with the fuel droplets to atomize, breakup aerodynamically and partially premix in a venturi nozzle before entering the combustor. The combination of the swirl and the venturi has proven to maximize the atomization performance and minimize the pressure drop across the injector (Im *et al.* (1998)). The venturi nozzle also provides the suitable residence time for the fuel droplets to vaporize and mix uniformly with the swirled air droplets. In the current paper, the single element

LDI will be simulated using an unstructured mesh. The results will be compared to the non-reactive experimental LDV data.

2. Numerical method

The simulation is performed by the unstructured LES code CDP. CDP is a set of massively parallel unstructured finite volume flow solvers developed specifically for large eddy simulation by Stanford's Center for Integrated Turbulence Simulations as part of the Department of Energy's ASC Alliance Program. The specific solver used to perform the simulations reported in this brief was the node-based incompressible flow solver `cdp_if2`, which solves the filtered incompressible Navier-Stokes equations:

$$\begin{aligned} \frac{\partial \overline{u_i}}{\partial x_j} &= 0.0 \\ \frac{\partial \overline{u_i}}{\partial t} + \frac{\partial \overline{u_i u_j}}{\partial x_j} &= -\frac{\partial \overline{P}}{\partial x_i} + \nu \frac{\partial \overline{u_i}}{\partial x_i \partial x_j} + \frac{\tau_{ij}}{\partial x_j} \end{aligned} \quad (2.1)$$

where τ_{ij} is the residual stress modeled by the dynamic Smagorinsky model Germano *et al.* (1991). The velocity u_i and the kinematic pressure p are collocated at the nodes. Time advancement uses a collocated fractional step method that implicitly introduces a 4th-order pressure dissipation to ensure proper velocity-pressure coupling. All other aspects of the discretization involve symmetric discretizations and are free from numerical dissipation. Details of the operators and the importance of minimizing numerical dissipation for LES can be found in Ham *et al.* (2006); Ham & Iaccarino (2004); Mahesh *et al.* (2004).

3. Numerical setup

The experimental setup and data is provided by Farhad *et al.* (2006). The geometry of the single element combustor is shown in Fig. 1. Liquid fuel is injected through the center (currently closed), while air is injected through a swirler with downstream vane angles of 60 degree. The swirler is composed of six helical vanes with an effective area of 870 mm². The fuel droplets from the centerline and the swirled air are mixed in a converging-diverging venturi nozzle.

An inflow bulk velocity of 20.14 m/sec is provided through a tube upstream of the swirl injector. For the non-reactive case, the inflow air is at temperature $T_o = 294$ K and pressure of 1 atm. The helical air swirler has an inside diameter of 9.3 mm and an outside diameter of 22.1 mm. The combustor has a square cross-sectional area of 44.2 mm. The mesh uses 1072,640 hexahedron elements, which is slightly above the 861,823 elements mesh used by Farhad *et al.* (2006). The unstructured mesh is shown in Fig. 2. The mesh distribution along the $Z=0.0$ plane and in the vanes is shown in Fig. 2-(a), while the $Y - Z$ plane grid distribution is in Fig. 2-(b). The mesh cells are clustered toward the centerline and toward the walls of the combustor. To achieve realistic inflow turbulence, the inflow cross section is extended three diameters upstream of the swirler, then the flow is cycled to the inlet from a cross-sectional area close to the swirlers. This procedure allows for a fully developed turbulent flow at the injector inlet with realistic inflow turbulence. The inflow mean and rms profile at the inflow section are shown in Fig. 3. The high, steep rms values close to the walls indicate the fully developed turbulent boundary layer.

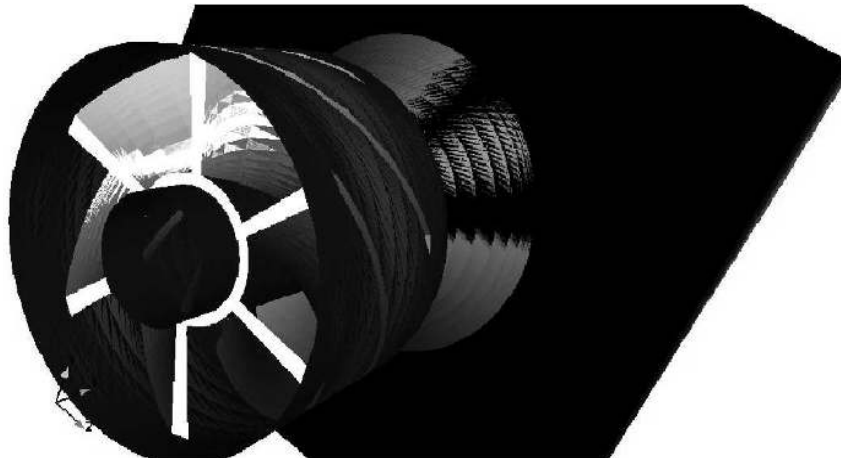
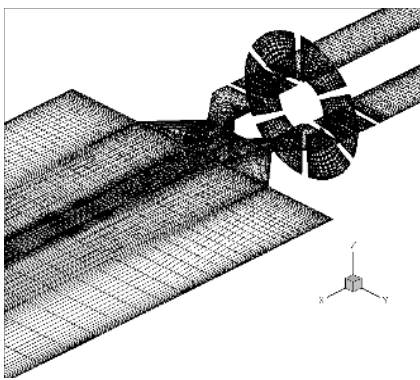
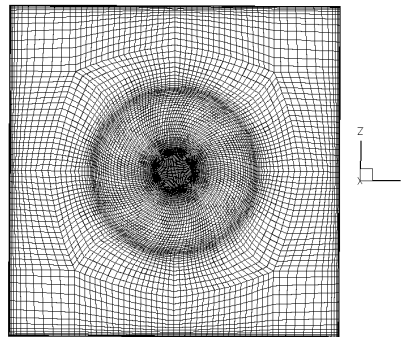


FIGURE 1. LDI single element geometry.



(a) The LDI mesh in the vanes and the venturi cross-section



(b) Y-Z mesh plane

FIGURE 2. The LDI unstructured hexahedron mesh.

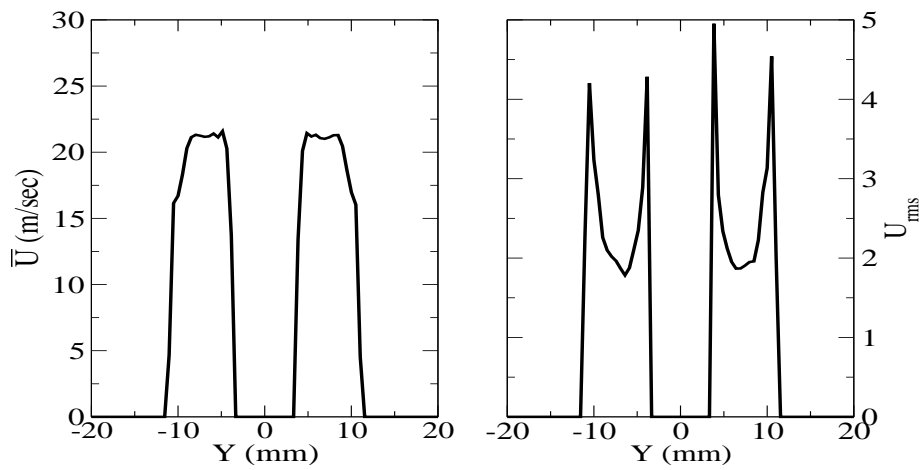


FIGURE 3. Inflow profile at the inlet of the vanes.

4. Results

In this section a comparison will be shown between the experimental LDV data and the LES results. The statistics are collected over 0.167 seconds. This is equivalent to 11 flow through times based on the inlet bulk velocity and the chamber length. Eight experimental locations are chosen for comparison. Some flow features will be shown first, then linear plots will be presented, followed by 2-D contour plots for the $Z - Y$ plane at each X location.

Figure 4 shows the mean axial velocity spectrum at different $Y - Z$ planes along the X -axis combined with the cut plane at $Z = 0.0$ for the axial velocity contours. The contour lines along the Z plane show that the accelerated flow in the convergent nozzle emerges with a very high spread cone angle and then expands toward the wall. The recirculation zone (RZ) established (discussed later) in the middle acts like a blockage, where the flow expands around it. This high spread rate will enhance the atomization process by collision of the high speed swirled air with the liquid particles emitted from the central jet (closed in this run). The jet collides with the walls and forms three recirculation zones: a big recirculation zone in the middle that extends radially about twice the chamber radius, another RZ at the corners and one close to the wall of the venturi. These three RZs are shown in Figs. 5 (a,b and c).

The middle recirculation zone length is shown numerically by comparing the centerline mean axial velocity in Fig. 5 (d) with the experimental results. Knowing that the error bar is on average ± 5 m/sec (see Farhad *et al.* (2006)), good agreement with the experimental results is observed. The RZ starts just downstream from the face of the injector and extends downstream of the venturi up until $X = 100$ mm. This long recirculation zone will anchor the flame, providing a strong static stability mechanism for combustion. The swirling flow merging from the venturi causes the shear stress between the particles to increase, which raises the adverse pressure gradient and establishes the RZ. The interaction between these recirculation zones will increase the flow unsteadiness and consequently will affect the ability to achieve the steady state in this region.

A zoom on the venturi area is shown in Fig. 6(a,b and c) and Fig. 7(a and b). Figures 6 shows the mean U_Y component at different cross sections from the vanes to just outside the venturi, while the axial component is shown in Fig. 7. The vanes rotate the flow in a counterclockwise wise direction (viewed from the exit side). The upper three vanes rotate the flow to the left and the lower three vanes rotate the flow to the right as shown in Fig. 6(a). Just downstream of the vanes in Fig. 6(b and c); inside the convergent divergent nozzle, the flow shows a complete solid body rotation in the counter-clockwise direction. As the flow passes, the convergent-divergent nozzle, the rotational packets are separated by a middle uniform flow and expand in the radial direction as shown in Fig. 6(d).

The flow inside the venturi and after the dump plane is presented in Fig. 7. The flow accelerates in the convergent part then eventually expands in the divergent part and after the dump plane around the RZ. The presence of the middle recirculation zone acts as a bluff body blockage where the flow expands around it. The swirl vanes cause the generation of six circumferential high-speed flow structures close to the wall followed by another six higher-speed smaller fluid packets in the radial direction toward the center and finally a central recirculation zone as shown in Fig. 7(a). The middle high speed structures are caused by the flow compression between the wall and middle recirculation zone. The outer high-speed structures are generated by the six vanes, which convect the flow in the axial direction while swirling it at the same time. These flow structures

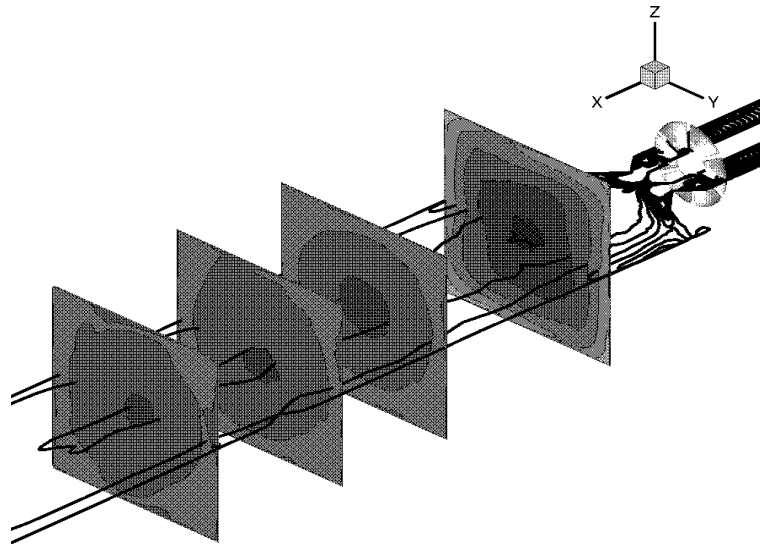


FIGURE 4. Mean axial velocity U_X along different $Y - Z$ planes and the middle Z plane.

merge together to form a single ring around the recirculation zone just downstream of the venturi as in Fig. 7(b).

The mean axial velocity for the plane $Y=0.0$ is shown in Fig. 8. Considering the range of confidence interval, the LES data shows good results in general. However, around $X = 3$ mm, the LES results shows wider shear layer, than the experiment. The peak shift is around 5 mm toward the wall. The flow at this location is highly unsteady with relatively high rms values (shown later). Slight over-prediction is also shown at the centerline as we go downstream at locations $X = 12$ mm, $X = 15$ mm, $X = 24$ mm and $X = 36$ mm. This over-prediction around $Z = 5$ mm is compensated by the under-prediction in the transverse speed (shown later).

The U_Z velocity component along the $Z=0.0$ plane is shown in Fig. 9. Good results are achieved at the different axial locations. The high transverse velocity shows the strong swirling effect of the air coming from the injector. The flow is rotated and swirled inside the RZ; this will enhance mixing and combustion. However, as shown experimentally, at the first three locations there are two flow packets that are rotating around the centerline. These packets expand slightly toward the centerline and then start to rotate around it. This behavior is due to the existence of the inner simplex injector at the inflow, which creates a low momentum flow area around the centerline, which represents the core of the RZ as shown in Fig. 8. The two rotating fluid packets start by rotating around this core, then expand toward the centerline around $X = 6$ mm. After $X = 6$ mm the rotational speed is not gaining any more strength other than expanding toward the wall. At $X = 48$ the flow close to the wall gains higher rotational speed from the inner flow and the whole cross-sectional area is rotating around the centerline. The data also has slight flow deviation at $Y = -5$ mm and $Y = 10$ mm; this indicates that the two flow rotational packets are rotating with higher speed than the experiment around the centerline. However, the rotational velocity of the fluid particles inside these packets are well predicted as shown in Fig. 10. Figure 10 shows the cross-stream velocity at the $Y = 0.0$ plane. At the locations

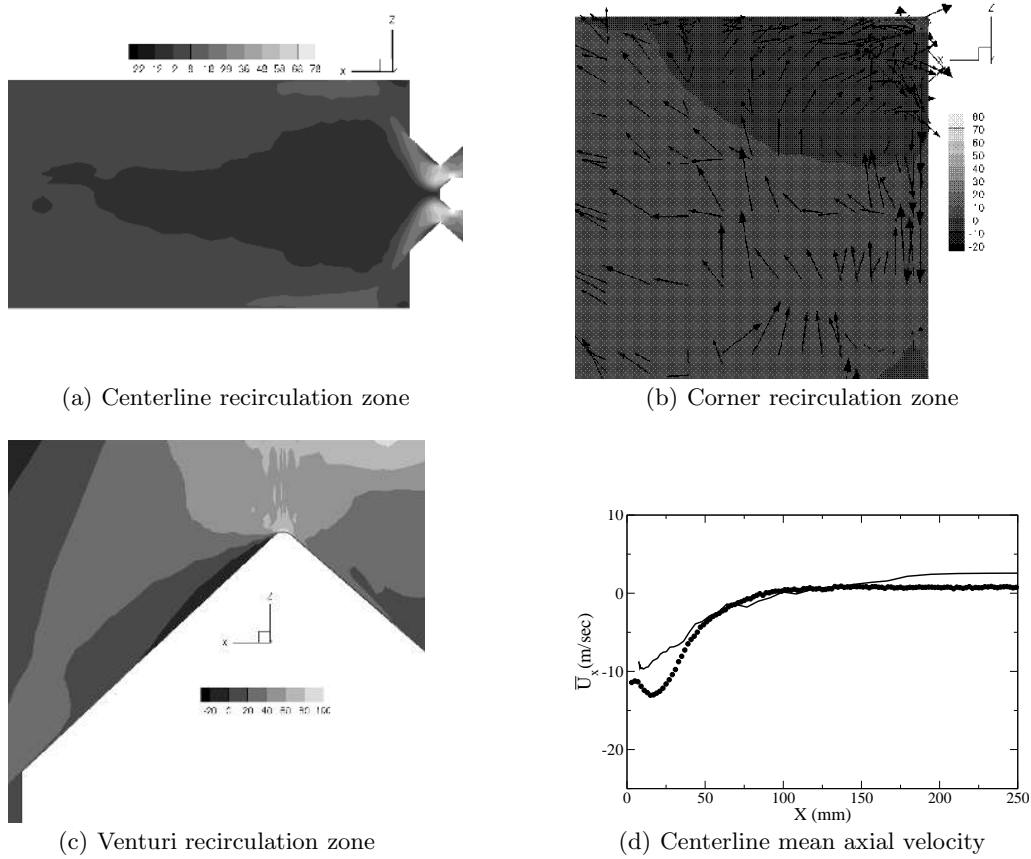


FIGURE 5. The LDI recirculation zones and centerline profile. (Experimental data \bullet , computational $-$).

where the U_Z velocity is over-predicted in Fig. 9, the cross-stream velocity U_Y is under-predicted. This makes sense from the continuity point of view as shown in Eq. (2.1). The decrease in the cross-stream velocity balances the overprediction in the axial velocity.

Since some discrepancy is noticed, especially at the location $X = 3$ mm, the rms profiles for the axial velocity are compared against experiment in Fig. 11. The rms values are very high at the first two locations, almost twice the mean values. This high rms reflects the high flow unsteadiness. The rms values at $X=3$ mm indicate that the shear layer predicted in LES is shifted radially about 4-3 mm in the wall direction, which explains the over-prediction seen in Fig. 8. The wider shear layer might be due to the grid stretching effect toward the wall. This wider shear layer can be explained by two means, the first is due to the merging of the six rotating flow packets shown earlier to form a more coherent structure than the experiment, and the second is the merging of the small shear layer generated at the tip of the dump exit and the shear layer at the outer edge of the RZ. This might need more grid resolution to be well captured. This also explains the inability to capture the shear layer growth toward the wall at the locations $X=15$ and $X=24$. As a result, the inflow from the venturi will have higher transverse and spanwise velocity as shown in Figs 9 and 10. As the fluid particles expand from

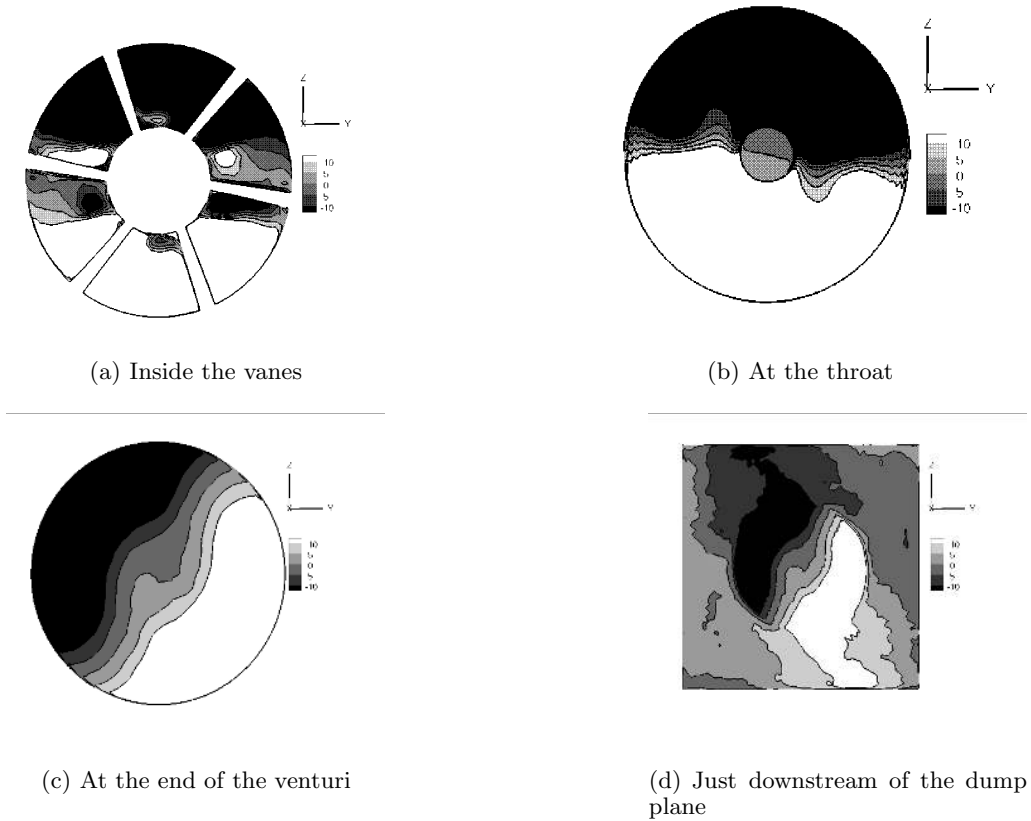
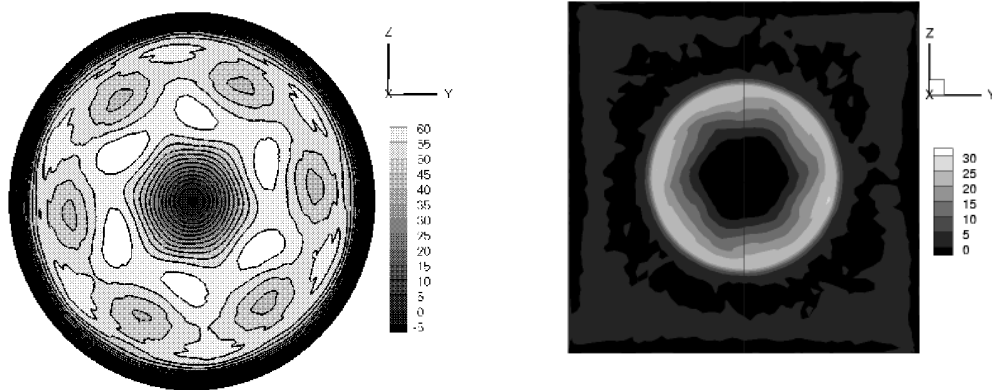


FIGURE 6. The mean U_Y velocity component in the venturi area.

the nozzle toward the wall, they experience smaller area passage than the experiment, and fluid particles are rotated with higher speed to compensate for the loss in the axial momentum. Another possible source of deviation is the blade thickness and orientation. While the orientation is adjusted to match the experiment as shown in Fig. 12, the blade thickness is harder to check, since no data is provided for the actual profile of the blade.

Figures 13, 14, and 15 compare the LES iso-contours of the mean axial velocity with the experimental LDV data at $X = 3$ mm, $X = 5$ mm, and $X = 12$ mm respectively. At $X = 3$ mm, the shear layer is wider than the experiment as previously explained. The six high-speed pockets are still represented in the experiment, while in LES they are smaller and nearly merged together. However, the inner RZ size and diameter compares well with the LDV data. In addition, the LES data shows more perturbations and smaller flow structures close to the chamber walls. The high flow unsteadiness at the locations close to the injector will promote the mixing process and will help achieve complete combustion by mixing the air and the atomized spray droplets. At $X = 5$ mm the flow features towards the wall are not well captured as previously mentioned. However, the shear layer growth rate looks similar to the experiment. The effect of the flow unsteadiness on the collected statistics diminishes at $X = 12$ mm, where the flow is more uniform in the radial direction and shows comparable results to the LDV data.

Finally, the mean radial velocity component is shown in Figs. 16, 17, and 18 respec-



(a) The mean axial velocity inside the venturi (b) The mean axial velocity just downstream of the venturi

FIGURE 7. The mean axial velocity across the venturi area.

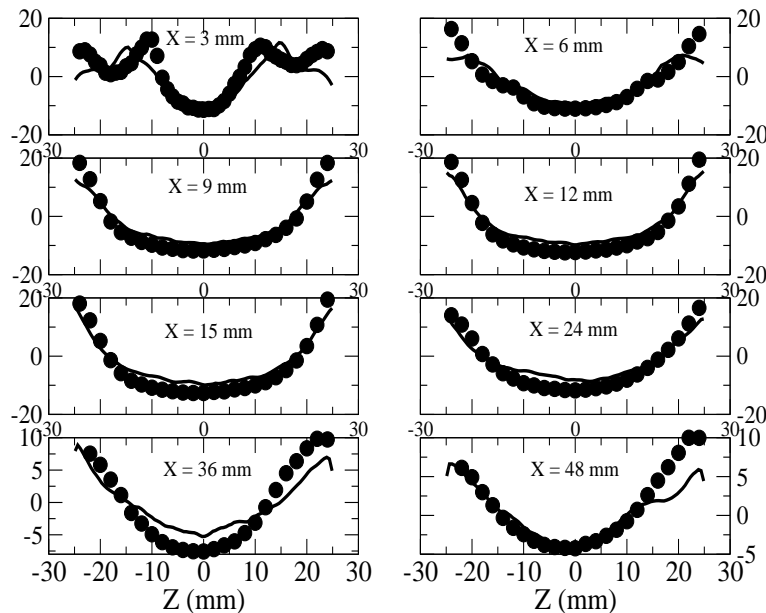


FIGURE 8. Comparison between the experimental (\bullet) and the LES computational results – for the mean axial velocity at the middle $Y=0.0$ plane.

tively. At $X=3$ mm, LES shows smaller rotating flow structures than the LDV data, with a middle uniform flow. This rotational flow is generated by the swirling vanes of the injector as previously mentioned. Further downstream, the rotational speed decreases. At the location $X=5$ mm the two solid-body rotations generated by the swirler expand in the radial direction, to finally form two large rotating structures near the lower and upper walls at $X=12$ mm. Both LES and LDV data shows zero rotational flow at the centerline, which expands toward the walls as the rotational speed becomes higher

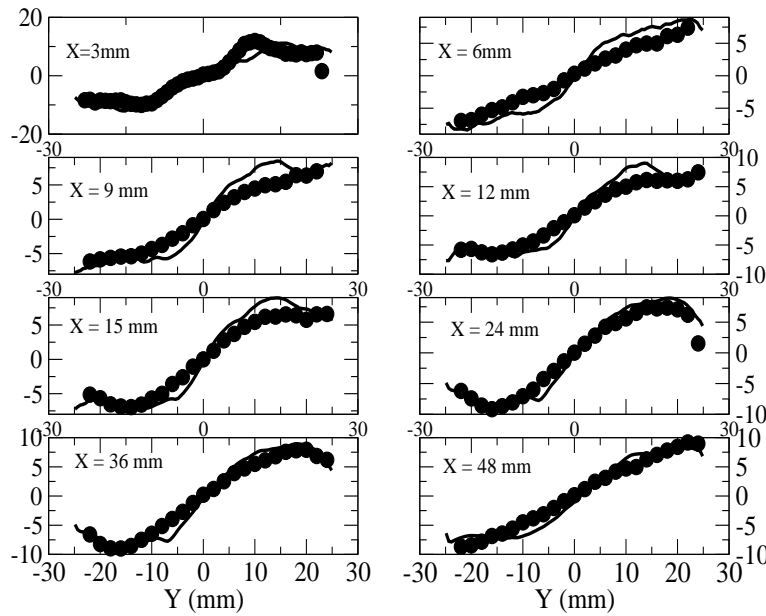


FIGURE 9. Comparison between the experimental (●) and the LES computational results – for the mean transverse velocity U_Z at the middle $Z=0.0$ plane.

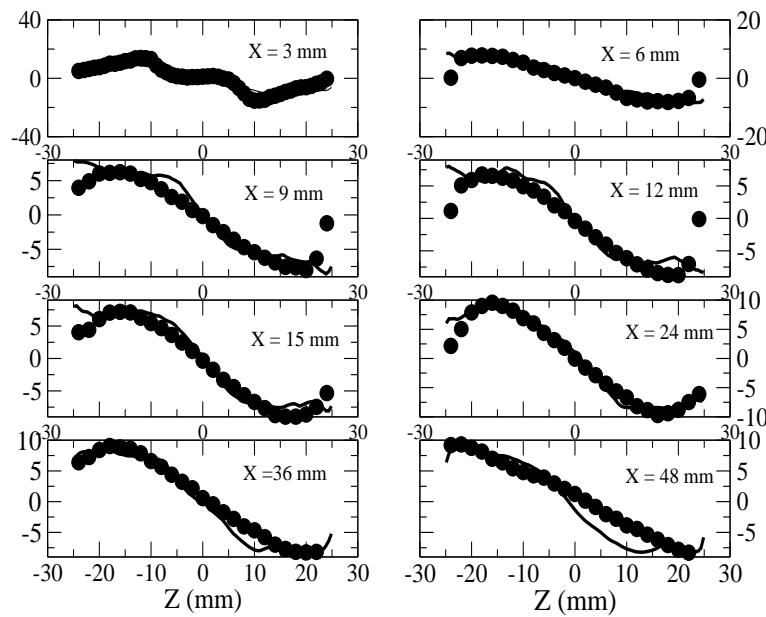


FIGURE 10. Comparison between the experimental (●) and the LES computational results – for the mean cross-stream velocity U_Y at the middle $Y=0.0$ plane.

toward the wall. The uniformity of the flow after this location is necessary to achieve a uniform temperature profile at the combustor exit, when ignition occurs.

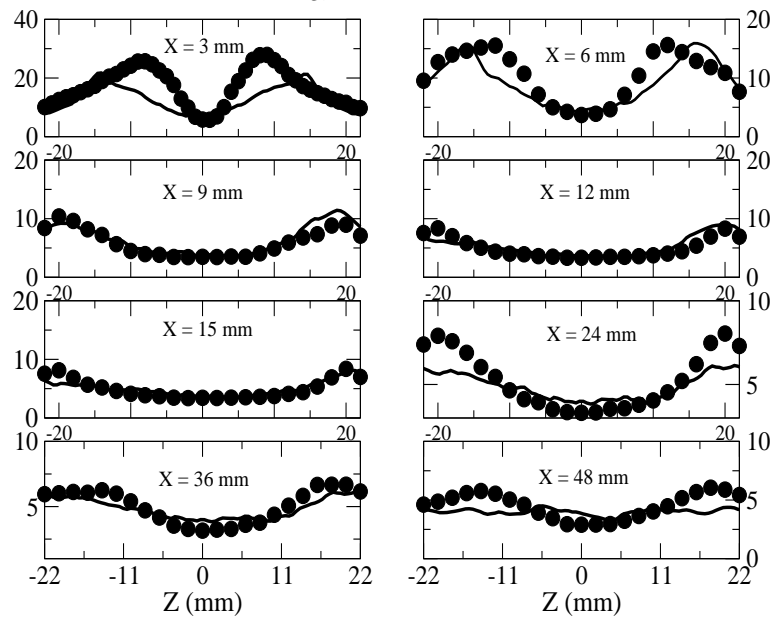
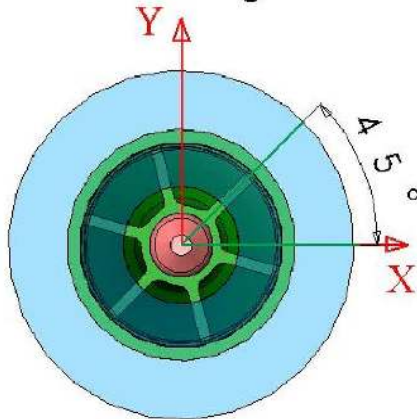
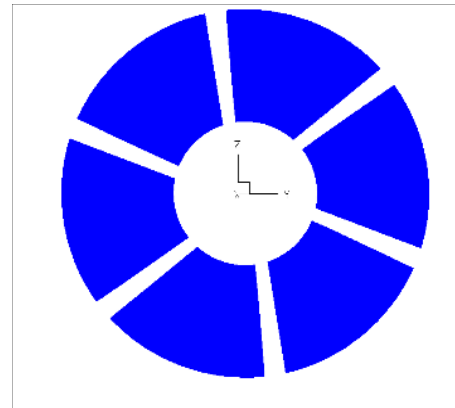


FIGURE 11. Comparison of the rms axial velocity (U_x) in-between the experiment (\bullet) and the LES ($-$) along the plane $Z = 0.0$.

Non-reacting Flow



(a) Experimental setup.



(b) LES setup.

FIGURE 12. Comparison of the swirler orientation.

5. Future work

The same test case will be implemented on a structured code using the immersed boundary technique. Since the numerical scheme is staggered in space and time, secondary conservation is guaranteed and higher-order accuracy can be achieved. Following that, more effort will be devoted to combustion multi-phase modeling and the development of more accurate and physical models to capture the flame/turbulence interaction and the flow physics in LES framework.

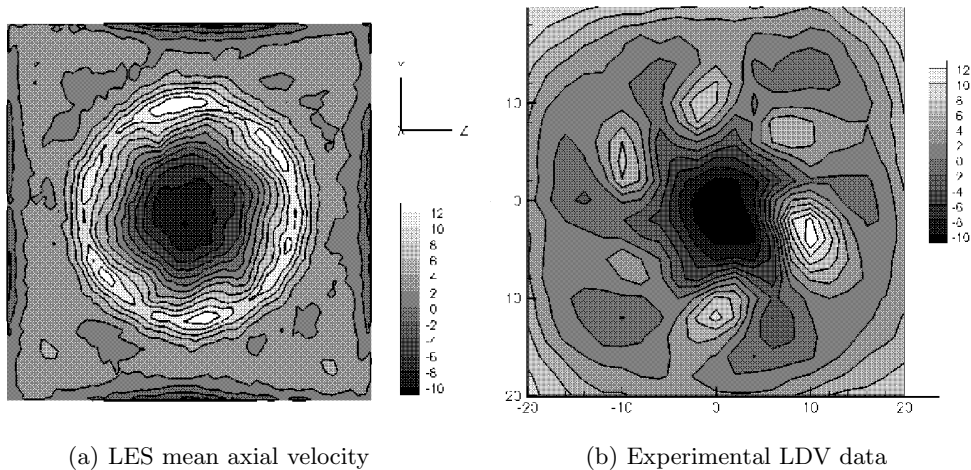


FIGURE 13. Comparison of the mean axial velocity (U_X) isocontours at $X = 3mm$.

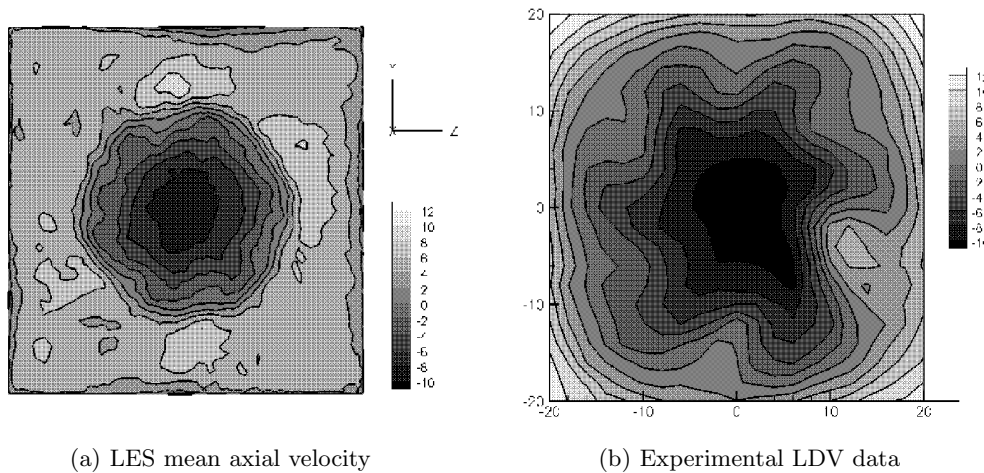


FIGURE 14. Comparison of the mean axial velocity (U_X) isocontours at $X = 5mm$.

6. Acknowledgments

The authors are thankful to Dr. Nan-Suey Liu for providing advice, grid and experimental data for comparison.

REFERENCES

- FARHAD D., NAN-SUEY, L., JEFFREY, P. M. 2006 Investigation of swirling air flows generated by axial swirlers in a flame tube. NASA/TM-2006-214252, GT2006-91300
- GERMANO, M., PIOMELLI, U., MOIN, P. & CABOT, W. H. 1991 A dynamic subgrid-scale eddy viscosity model. *Phys. Fluids A* **3** 17601765.
- HAM, F. & IACCARINO, G. 2004 Energy conservation in collocated discretization schemes on unstructured meshes. Annual Research Briefs 2004. Center for Turbulence Research, Stanford University / NASA Ames.

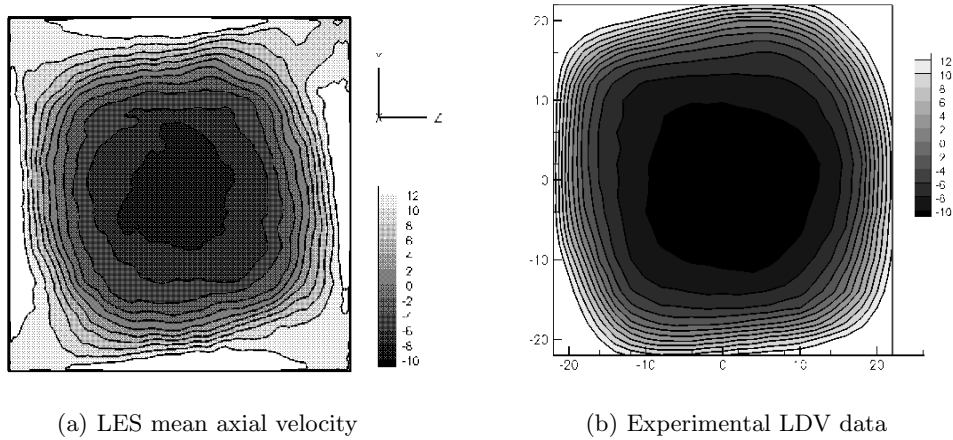


FIGURE 15. Comparison of the mean axial velocity (U_x) isocontours at $X = 12mm$.

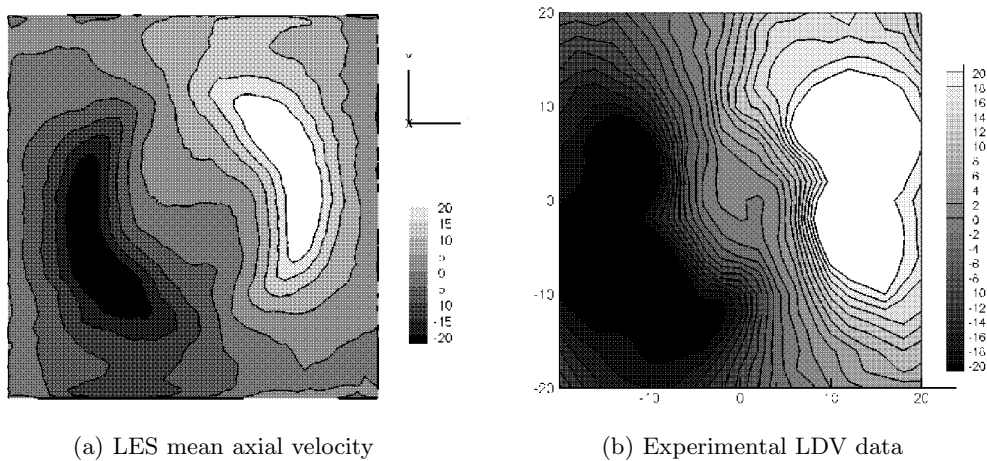


FIGURE 16. Comparison of the mean radial velocity (U_z) isocontours at $X = 3mm$.

- HAM, F., MATTSSON, K. & IACCARINO, G. 2006 Accurate and stable finite volume operators for unstructured flow solvers. Annual Research Briefs 2006. Center for Turbulence Research, Stanford University.
- IM, K.-S., LAI, M. C., TACINA, R. R. 1998 A parametric spray study of the swirler/venturi injectors. AIAA/ASME/SAE/ASEE Joint Propulsion Conference and Exhibit, 34th, Cleveland, Ohio AIAA 98-3269.
- JUN, C., JENG, S.-M., TACINA, R. R. 2005 The structure of a swirl-stabilized reacting spray issued from an axial swirler. AIAA Aerospace sciences meeting and exhibit, 43rd, Reno, Nevada AIAA 2005-1424.
- MAHESH, K., CONSTANTINESCU, G. & MOIN, P. 2004 A numerical method for large-eddy simulation in complex geometries. *J. Comput. Phys.* **197**, 215–240.
- TACINA, R. R., WEY, C., CHOI, K. J. 2001 Flame tube NO_x emissions using a lean-

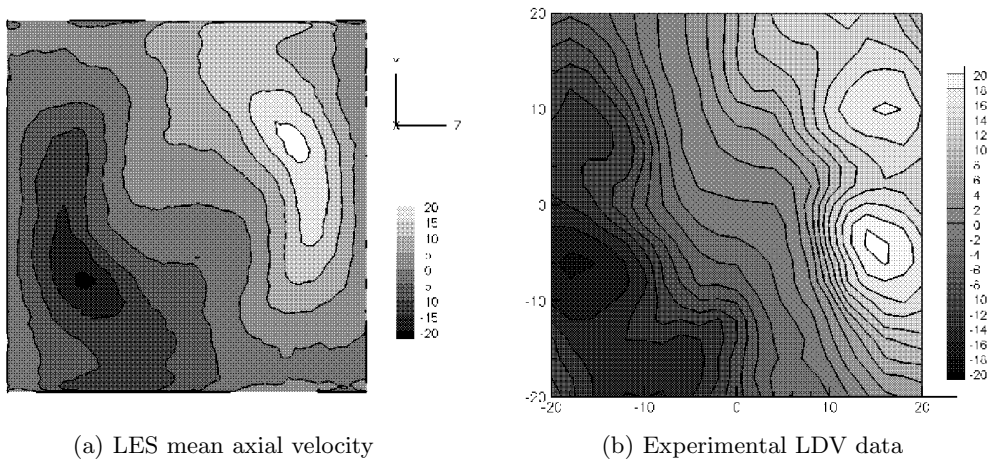


FIGURE 17. Comparison of the mean radial velocity (U_z) isocontours at $X = 5mm$.

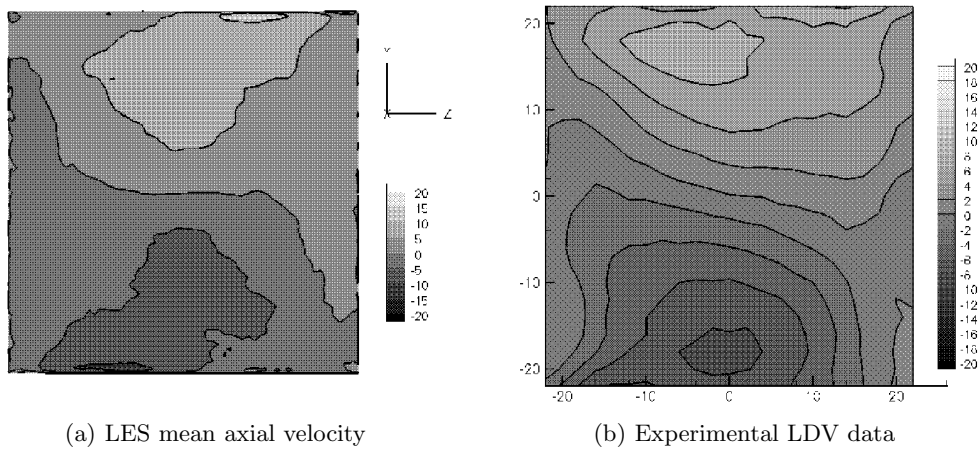


FIGURE 18. Comparison of the mean radial velocity (U_z) isocontours at $X = 12mm$.

direct-wall-injection combustor concept. AIAA/ASME/SAE/ASEE Joint propulsion conference and exhibit, 37th, Salt Lake City, Utah AIAA 2001-34065.

YANG, S. L., SIOW, Y. K., PESCHKE, B. D., TACINA, R. R. 2003 Numerical study of nonreacting gas turbine combustor swirl flow using Reynolds stress model J. Eng. Gas Turb. Power **125**, 804–811.